Dalton Transactions

ROYAL SOCIETY OF CHEMISTRY

PAPER

View Article Online
View Journal | View Issue

Cite this: *Dalton Trans.*, 2025, **54**, 2166

Giant {Mo_{132}} polyoxometalate isolated with diverse organic cations: a systematic proton conductivity study†

Parvathy M. Unnikrishnan,‡ Olivia Basu,‡ Rajendar Nasani and Samar K. Das *

The development of efficient and stable proton conductors is a pivotal area of research due to their transformative potential in alternative energy technologies. Recently, there has been a surge of interest in synthesizing proton conductors based on polyoxometalate (POM) materials, attributed to their highly negatively charged and oxygen-rich surfaces. In this study, we report on a highly water-soluble giant POM, $(NH_4)_{42}[Mo_{132}O_{372}(CH_3COO)_{30}(H_2O)_{72}]\cdot ca.300H_2O\cdot ca.10CH_3COONH_4$ (designated as {Mo_{132}}), which was rendered insoluble in water by exchanging its ammonium cations with larger organic cations, specifically histidinium, pyridinium, bipyridinium, and methyl viologen, resulting in **His-Mo_{132}**, **Py-Mo_{132}**, **Bpy-Mo_{132}** and **MV-Mo_{132}**, respectively. These ion-exchanged compounds were thoroughly characterized through comprehensive spectral analyses, elemental analyses and microscopic studies. The substitution with organic cations containing nitrogen centres not only rendered {Mo_{132}} insoluble, but also increased the number of proton hopping sites, thereby enhancing proton transport. Consequently, **His-Mo_{132}**, **Py-Mo_{132}**, **Bpy-Mo_{132}** and **MV-Mo_{132}** demonstrated impressive proton conductivity. Among these, **Py-Mo_{132}** stood out with a proton conductivity of 1.07×10^{-2} S cm^{-1} under 98% relative humidity at 80 °C. All four compounds exhibited proton conduction predominantly *via* the Grotthuss mechanism. Furthermore, stability assessments of these Mo_{132}-based proton conductors were conducted under operational conditions to evaluate their performance in practical applications.

Received 9th October 2024,
Accepted 9th December 2024

DOI: 10.1039/d4dt02834a

rsc.li/dalton

Introduction

The current global energy demands necessitate a thorough understanding and management of energy resources. With depleting fossil fuels and increasing pollution from a growing population, research on sustainable energy sources is crucial. Some of the cleaner energy devices are fuel cells, which use a redox reaction to convert chemical energy to electrical energy.[1–4] Among different types of fuel cells, proton exchange membrane fuel cells or polymer electrolyte membrane fuel cells (PEMFCs) use a solid electrolyte as a proton conducting membrane.[5–8] Nafion, a synthetic polymer with terminal sulfonic acid groups, is widely used in PEMFCs due to its high proton conductivity under humid conditions.[9,10] However, Nafion's performance degrades at temperatures above 100 °C due to dehydration, breaking proton transport channels and reducing conductivity.[11,12] Additionally, Nafion's high cost drives the need for new proton-conducting materials that are more affordable, effective over a broader temperature range, and highly efficient for use in fuel cells.[13]

Polyoxometalates (POMs),[14–20] metal–organic frameworks (MOFs),[21,22] covalent organic frameworks (COFs),[23–25] graphene oxide,[26,27] and perovskites[28,29] are notable materials that have recently proven effective in developing efficient proton conductors. Each class has unique properties that make them suitable candidates for proton conduction. POMs, composed of metal–oxygen clusters from early transition metals, stand out due to their oxygen-enriched surfaces, Lewis and Brønsted acidity, electron-accepting ability, and customizable synthesis.[14–20] Along with these, their high negative charge also contributes to their efficiency as proton conductors.[30–41] However, POMs' high solubility in water and low structural stability in solution limit their use in proton exchange membranes (PEMs).[31,32] To address this, strategies such as incorporating POMs with materials like TiO_2, SiO_2, and ZrO_2, and ion exchange with organic cations have been developed.[42–45]

Nakamura *et al.* first conducted a detailed study of the proton conductivity of POMs, specifically dodecamolybdophosphoric acid ($H_3PMo_{12}O_{40}\cdot 29\ H_2O$) and dodecatungstopho-

School of Chemistry, University of Hyderabad, Hyderabad – 500046, India.
E-mail: skdas@uohyd.ac.in

†Electronic supplementary information (ESI) available. See DOI: https://doi.org/10.1039/d4dt02834a

‡These authors contributed equally to this work.

sphoric acid ($H_3PW_{12}O_{40}\cdot 29\cdot H_2O$).[30] In recent years, numerous reports on POM-based proton conductors have emerged. Wang *et al.* reported assembling discrete POM units into a 3-D inorganic framework to enhance proton conductivity and stability.[32] Our group has reported two polyoxovanadate-based materials with acidic protons as cations, exhibiting proton conductivity on the order of 10^{-3} S cm^{-1} under mild conditions (50 °C and 70% RH).[33] Lin *et al.* described a POM with a high nuclearity hollow dodecahedron cage, showing proton conductivity between 10^{-2} and 10^{-1} S cm^{-1} over a wide temperature range.[34] Recently, Supriya and co-workers reported a sparingly water soluble giant POM, $\{Mo_{72}Fe_{30}\}[Mo_{72}Fe_{30}O_{252}(CH_3COO)_{12}\{Mo_2O_7(H_2O)\}_2\{H_2Mo_2O_8(H_2O)\}(H_2O)_{91}]\cdot 150H_2O$, exhibiting proton conductivity on the order of 10^{-3} S cm^{-1} under moderate humidity (R.H. 50%) and temperature (<50 °C) conditions.[35]

The family of giant Keplerate-type polyoxometalates emerged in 1998. $\{Mo_{132}\}$, bearing the formula $(NH_4)_{42}[Mo_{132}O_{372}(CH_3COO)_{30}(H_2O)_{72}]\cdot ca.300H_2O\cdot ca.10CH_3COONH_4$, is a well-known member of this family.[46] It has a spherical shape with icosahedral symmetry and a diameter of ~2.9 nm. This giant $\{Mo_{132}\}$ polyanion consists of 12 $\{Mo_{11}\}$ fragments with central Mo^{VI} existing as an $Mo^{VI}O_7$ pentagonal bipyramid. This unit is then surrounded by 5 $Mo^{VI}O_6$ octahedral groups. Each of these 12 $\{(Mo)Mo_5\}$ units is connected to each other by 30 Mo_2^v linkers, stabilized by bidentate acetate ligands, to form a giant sphere. Each $\{Mo_{132}\}$ polyanion carries 42 negative charges, which is balanced by 42 ammonium cations. The ammonium cations in the structure and the numerous oxygen atoms on the POM surface, which can engage in extensive hydrogen bonding, make $\{Mo_{132}\}$ an excellent candidate for study as a proton conductor. However, its high water solubility is a significant challenge. To address this, one can utilize the large hollow cage structure of the $\{Mo_{132}\}$ anion, which can host smaller cations. Using this strategy, Neumann and his team encapsulated first-row transition metals within $\{Mo_{132}\}$ and replaced the NH_4^+ cations with quaternary ammonium cations, making the system water-insoluble.[47]

Another effective method is the ion exchange of NH_4^+ cations in $\{Mo_{132}\}$ with organic cations, as demonstrated by Lan and co-workers.[48] They synthesized a series of insoluble $\{Mo_{132}\}$ systems using imidazolium cation derivatives and a tetrabutylammonium cation, producing $HImMo_{132}$, $HMeImMo_{132}$, $ILMo_{132}$ and $TBAMo_{132}$, which primarily operated *via* the vehicular mechanism of proton conduction. This work encouraged us to explore the role of diverse organic cations that can be exchanged with the NH_4^+ cations of parent NH_4^+-$\{Mo_{132}\}$ to form $\{Mo_{132}\}$-based proton conductors. The diversity of organic cations, in terms of the pK_a value and the number and type of nitrogen atoms, has provided useful insights into the proton conducting behaviour of these systems.

Keeping this view in mind, in this study, we report the synthesis, characterization, and proton conducting properties of four new water-insoluble $\{Mo_{132}\}$-based compounds: **His-Mo$_{132}$**, **Py-Mo$_{132}$**, **Bpy-Mo$_{132}$**, and **MV-Mo$_{132}$**, derived from histidine (His), pyridine (Py), bipyridine (Bpy), and its dicationic methylated analogue, methyl viologen (MV^{2+}), respectively. A schematic illustration of the preparation of these products is shown in Scheme 1. Here, it is to be noted that pyridine has one N-center, bipyridine and methyl viologen have two, and histidine has three N-centers along with a carboxylic acid group. The choice of these organic molecules offers an interesting series of compounds, providing insights into the role of nitrogen heteroatoms and cations in modifying proton conductivity.

Experimental section

The synthetic procedure for the ion-exchanged products, **Py-Mo$_{132}$**, **Bpy-Mo$_{132}$**, **MV-Mo$_{132}$** and **His-Mo$_{132}$**, was adapted from the work of Lan and co-workers.[48] Even though it is known that the strong hydration shell of smaller ammonium cations present in the solution prevents other organic cations from directly interacting with the $\{Mo_{132}\}$ polyanion having a low charge density,[49] the excess concentration of organic cations ultimately results in the exchange of some of the ammonium ions, forming new water insoluble $\{Mo_{132}\}$ complexes. The detailed procedures are provided below. The synthesis pro-

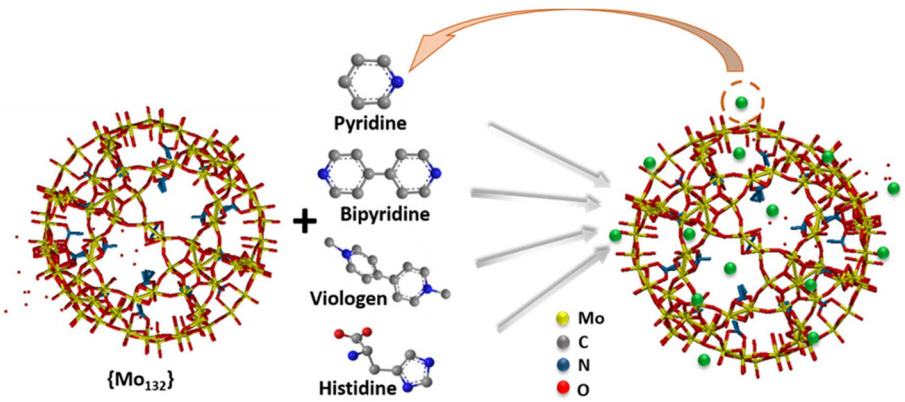

Scheme 1 Schematic representation of the formation of **Py-Mo$_{132}$**, **Bpy-Mo$_{132}$**, **MV-Mo$_{132}$** and **His-Mo$_{132}$**.

cedures of pristine {Mo_{132}} and methyl viologen are provided in the ESI (Section S1†).

Synthesis of $(NH_4)_{13}(PyH)_{29}[Mo^{VI}_{72}Mo^{V}_{60}O_{372}(CH_3COO)_{30}(H_2O)_{72}]\cdot 77H_2O$: (Py-$Mo_{132}$)

0.3 mL of pyridine (3 mmol) was mixed with 3 mL of water, and the pH was adjusted to 4.0 using glacial acetic acid. To this solution, 0.8 g of {Mo_{132}} (0.03 mmol) was added, which immediately resulted in the precipitation of the ion exchanged product. A dark brown colored product was filtered after stirring for 5 minutes, washed with water, and dried in air. Yield: 0.67 g (83% based on Mo).

IR (cm^{-1}): 1607(m: δ_{CH_3}), 1536(m: ν_{COO^-}), 1487(m: $\delta_{NH_4^+}$), 1403(br, m), 1329(w), 1249(w), 945(ν(Mo═O)), 771(w), 660(w).

Elemental CHN (carbon, hydrogen and nitrogen) analysis (EA) of $C_{225}H_{664}N_{52}O_{591}Mo_{132}$ (MW – 26 219.73): % calcd (found): C 9.61(9.8), H 2.41(2.6), N 2.30(1.63); inductively coupled plasma (ICP) analysis % calcd (found): Mo 48.30(52). The number of pyridinium ions was calculated to be 29 by ICP-OES analysis and CHN analysis.

Synthesis of $(NH_4)_{20}(HisH)_{22}[Mo^{VI}_{72}Mo^{V}_{60}O_{372}(CH_3COO)_{30}(H_2O)_{72}]\cdot 110H_2O\cdot 10CH_3COONH_4$: His-$Mo_{132}$

0.232 g of histidine (1.5 mmol) was dissolved in 3 mL of water and the pH of the solution was adjusted to 4.0 using glacial acetic acid. 0.8 g of {Mo_{132}} (0.03 mmol) was then added to the solution and stirred for 5 minutes. A dark brown colored product was filtered, washed with water, and dried in air. Yield: 0.69 g (88% based on Mo).

IR (cm^{-1}): 1614(w: δ_{CH_3}), 1533(w: ν_{COO^-}), 1403(m: $\nu_{NH_4^+}$), 1326(w), 970(ν(Mo═O)), 787(vs), 697(vs).

Elemental CHN (carbon, hydrogen and nitrogen) analysis (EA) of $C_{212}H_{802}N_{96}O_{678}Mo_{132}$ (MW – 28 210.92): % calcd (found): C 9.03(10.08), H 2.87(2.69), N 4.77(4.42); ICP analysis % calcd (found): 44.89(47.5). The number of histidinium ions was calculated to be 22 from ICP-OES analysis and CHN analysis.

Synthesis of $(NH_4)_{18}(BpyH)_{24}[Mo^{VI}_{72}Mo^{V}_{60}O_{372}(CH_3COO)_{30}(H_2O)_{72}]\cdot 128H_2O\cdot 10CH_3COONH_4$: Bpy-$Mo_{132}$

0.234 g of bipyridine (1.5 mmol) was dissolved in 3 mL of water and the pH of the solution was adjusted to 4.0 using glacial acetic acid. To this solution, 0.8 g of {Mo_{132}} (0.03 mmol) was added and stirred. A dark brown precipitate formed immediately, which was then filtered, washed with water and dried in air. Yield: 0.71 g (88% based on Mo).

IR (cm^{-1}): 1614(m: δ_{CH_3}), 1539(m: ν_{COO^-}), 1484(w), 1410(m: $\nu_{NH_4^+}$), 1205(w), 948(w): (ν(Mo═O)), 846(w), 784(vs), 697(vs).

Elemental CHN (carbon, hydrogen and nitrogen) analysis (EA) of $C_{320}N_{76}H_{848}O_{652}Mo_{132}$ (MW – 28 858.32): % calcd (found): C 13.32(13.79), H 2.96(2.63), N 3.69(3.02); ICP analysis % calcd (found) 43.8(47). The number of bipyridinium ions was calculated to be 24 from ICP-OES analysis and CHN analysis.

Synthesis of $(NH_4)_{14}(MV)_{14}[Mo^{VI}_{72}Mo^{V}_{60}O_{372}(CH_3COO)_{30}(H_2O)_{72}]\cdot 94H_2O$: MV-$Mo_{132}$

0.330 g of methyl viologen (0.75 mmol) was dissolved in 3 mL of water. The pH of this solution was already at 3.0, so it did not require acidification. To this solution, 0.8 g of {Mo_{132}} (0.03 mmol) was added and stirred for 5 minutes. A dark brown product was then filtered, washed with water and dried in air. Yield: 0.64 g (85% based on Mo).

IR (cm^{-1}): 1645(m: δ_{CH_3}), 1546(w: ν_{COO^-}), 1428(m: $\nu_{NH_4^+}$), 1329(w), 1267(w), 1186(s), 948(w): (ν(Mo═O)), 901(w), 787(m), 703(m)

Elemental CHN (carbon, hydrogen and nitrogen) analysis (EA) of $C_{248}H_{724}N_{52}O_{608}Mo_{132}$ (MW – 26 828.44): % calcd (found); C 10.44(11.01), H 2.59(2.86), N 2.24(1.7); ICP-OES analysis % calcd (found): 52.4(47.2). The number of methyl viologen ions was calculated to be 14 from ICP-OES analysis and CHN analysis.

Physical characterization studies

The products were characterized using different analytical techniques such as IR spectroscopy, powder X-ray diffraction (PXRD), Raman spectroscopy, thermogravimetric analysis (TGA), field emission scanning electron microscopy (FESEM), UV-visible spectroscopy, elemental analyses [inductively coupled plasma optical emission spectrometry (ICP-OES) and carbon, hydrogen and nitrogen (CHN) elemental analysis], dynamic vapor sorption (DVS) and X-ray photoelectron spectroscopy (XPS). PXRD was performed using a PANalytical X'Pert^3 powder instrument, and data were analyzed using Bruker DIFFRAC plus EVA software. Raman spectra were obtained with the help of a HORIBA LabRAM HR800 instrument using a 633 nm argon ion laser. IR spectroscopy was performed using an iD7 ATR Thermo Fisher Scientific Nicolet iS5 instrument. TGA was performed using a PerkinElmer Simultaneous Thermal Analyzer STA-6000. The samples were heated from 30 °C to 800 °C at 10 °C per minute. FESEM imaging was done using a Carl Zeiss model Ultra 55 microscope. Before imaging, all the samples were gold-coated. Diffuse reflectance UV-visible spectroscopy was carried out using a Shimadzu 2600 spectrophotometer. CHN analysis was conducted using a Thermo Scientific FLASH 2000 HT analyzer and ICP-OES analysis was performed using a PerkinElmer Optima 5300 DV ICP-OES. DVS analysis was conducted using a TA Q5000 SA instrument under a N_2 atmosphere at a temperature of 25 °C. Methyl viologen synthesized was analyzed by IR spectroscopy and liquid chromatography-mass spectrometry (LC-MS). LC-MS analysis was performed using a Shimadzu LCMS-8040 instrument.

Electrochemical impedance spectroscopy (EIS)

The proton conductivity of all the samples was studied using electrochemical impedance spectroscopy. Prior to the measurement, the samples were powdered well, and 400 mg of

each powdered sample was made into a pellet by placing it between two carbon papers in a pellet maker and applying 3 tons of pressure for 2 minutes. The pellet's thickness was measured using a screw gauge, and the contact surface area was also calculated.

The pellet was then placed between two stainless-steel electrodes, ensuring contact with the carbon papers. For temperature-dependent studies, the setup was placed in a 5 L sealed flask with circulating hot air and distilled water at the bottom. The temperature inside the flask was monitored with a digital thermometer. Impedance spectra were recorded at ≥95% relative humidity and temperatures ranging from 35 °C to 80 °C. Humidity-dependent impedance measurements were conducted in a programmable humidity chamber, keeping the temperature constant while varying the humidity.

Results and discussion

The synthesized products were characterized using various spectroscopic techniques and the data obtained were compared with those of parent {Mo_{132}}, as and when required. To estimate the number of remaining NH_4^+ cations and exchanged organic cations for each of the products, CHN and ICP analyses were performed. All the products were then studied for proton conductivity. The mechanism of proton transfer and the stability of the materials under the operational conditions were evaluated.

The IR spectra of all the products, **Py-Mo$_{132}$**, **His-Mo$_{132}$**, **Bpy-Mo$_{132}$** and **MV-Mo$_{132}$**, and parent {Mo_{132}}, are shown in Fig. 1a. For all the samples, two clusters of peaks can be observed: one in the 1650–1350 cm^{-1} range and the other in the 970–600 cm^{-1} range. The characteristic peaks of {Mo_{132}}, originating from the asymmetric stretching of Mo–O–Mo bridges and the asymmetric stretching of terminal Mo=O bonds, can be observed at ~784 cm^{-1} and ~950 cm^{-1}, respectively, for all the samples.[46,47] The stretching of $-COO^-$ and NH_4^+ groups is represented by the relatively weak bands at 1542 cm^{-1} and 1401 cm^{-1}, respectively, in all the spectra. This shows that the structure of the {Mo_{132}} anion remains intact in all the cation exchanged products. Now, since all the organic cations chosen are aromatic in nature with C=C bonds, its presence can be confirmed by the peak at 1625 cm^{-1}. The broad band in the range of 3100–3600 cm^{-1} (see ESI, Section S2.6†) represents the O–H stretch along with the aromatic C–H bonds. In addition to it, the presence of the characteristic peaks at ~1480 cm^{-1} and ~1250 cm^{-1}, originating from the N–H bending modes of aromatic secondary amine and C–N bonds, further confirms the presence of organic cations in the products.

The Raman spectra of the four products, **Py-Mo$_{132}$**, **His-Mo$_{132}$**, **Bpy-Mo$_{132}$**, **MV-Mo$_{132}$**, and {Mo_{132}}, are shown in Fig. 1b. For {Mo_{132}}, the two most prominent peaks appear at ~820 cm^{-1} and ~993 cm^{-1}. The peak at ~820 cm^{-1} originates from the symmetric breathing of oxygen atoms connecting the {(Mo)Mo_5} units with Mo_2^V units in the {Mo_{132}} ball.[50,51] A stretching of the terminal oxygen atoms (Mo=O) in the {Mo_{132}} ball generates the peak at ~993 cm^{-1} in the spectrum. The peak at ~650 cm^{-1} with very low intensity is due to the scissoring motion of bridging oxygen atoms. Another peak of medium intensity is observed at ~345 cm^{-1}, originating from the bending motion of pentagon non-terminal oxygen atoms. In the Raman spectra of **Py-Mo$_{132}$**, **His-Mo$_{132}$**, **Bpy-Mo$_{132}$**, and **MV-Mo$_{132}$**, the positions and intensities of the peaks corresponding to the {Mo_{132}} ball are similar to those in pristine {Mo_{132}}, which indicates the preservation of the {Mo_{132}} ball (icosahedral cluster) in all four products.

The powder X-ray diffraction (PXRD) pattern of the synthesized {Mo_{132}} matches well with the simulated pattern (Fig. S3, ESI†). The PXRD patterns of the four ion-exchanged

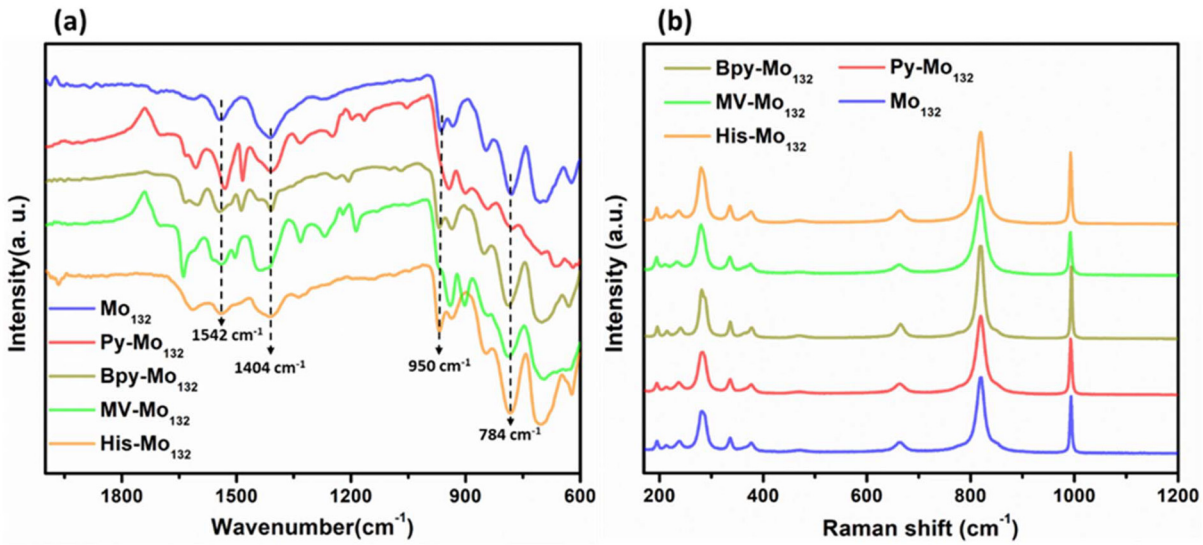

Fig. 1 (a) Infrared spectra and (b) Raman spectra of **Py-Mo$_{132}$**, **His-Mo$_{132}$**, **Bpy-Mo$_{132}$**, **MV-Mo$_{132}$** and pristine {Mo_{132}}.

products, **Py-Mo$_{132}$**, **His-Mo$_{132}$**, **Bpy-Mo$_{132}$**, and **MV-Mo$_{132}$**, provided in Fig. 2, show that the products are crystalline in nature. A careful analysis of these reveals that the patterns for ion-exchanged products are similar to that of pristine {Mo$_{132}$} but not identical to it in the sense that there are differences in the relative intensity of the peaks. The exchange of the NH_4^+ ions in pristine {Mo$_{132}$} with the larger organic cations, probably and quite expectantly, caused this discrepancy compared to pristine {Mo$_{132}$}. The overall similarity of the PXRD patterns of the synthesized ion-exchanged compounds with that of parent {Mo$_{132}$} indicates that the title compounds crystallize in the same crystal system as that of pristine {Mo$_{132}$}. Indeed, we were successful in obtaining the unit cell parameters of the single crystals for two such compounds, **Py-Mo$_{132}$** and **His-Mo$_{132}$**, both belonging to the cubic crystal system, which is the crystal system of the parent {Mo$_{132}$} molecule, the details of which are provided in the ESI (Section S2.3†). This again suggests that {Mo$_{132}$} retains its structure, *i.e.*, the cubic crystal system, in the ion-exchanged products in the present study.

To further verify whether the ion-exchanged products are indeed new crystalline ion-exchanged materials and not a physical mixture of the starting materials, we did a comparative analysis of these products with their respective starting organic molecules and pristine {Mo$_{132}$} using PXRD and FT-IR spectroscopy. The obtained results have been provided in the ESI (Sections S2.4 and S2.6†). From Fig. S4 (ESI†), it can be observed that the PXRD patterns of **His-Mo$_{132}$**, **Bpy-Mo$_{132}$** and **MV-Mo$_{132}$** do not contain any characteristic peak from their respective parent organic molecules, indicating that the synthesized products are not physical mixtures.

However, here it is interesting to find that the IR spectra of all the ion-exchanged products (Fig. S7, ESI†) show the characteristic features of both {Mo$_{132}$} and the parent organic molecules, along with the generation of several new peaks. From the results obtained for these experiments, we can safely conclude that the products **Py-Mo$_{132}$**, **His-Mo$_{132}$**, **Bpy-Mo$_{132}$** and **MV-Mo$_{132}$** are not physical mixtures of their starting materials, but indeed new crystalline ion-exchanged materials.

The UV-visible absorption spectra of parent {Mo$_{132}$} and the ion-exchanged products were recorded, and no notable changes were observed in the higher wavelength region of 450 nm–750 nm, which corresponds to the Mo^V d–d transition and Mo^V–Mo^{VI} inter-valence charge transfer transition (Section S2.7, ESI†).[52]

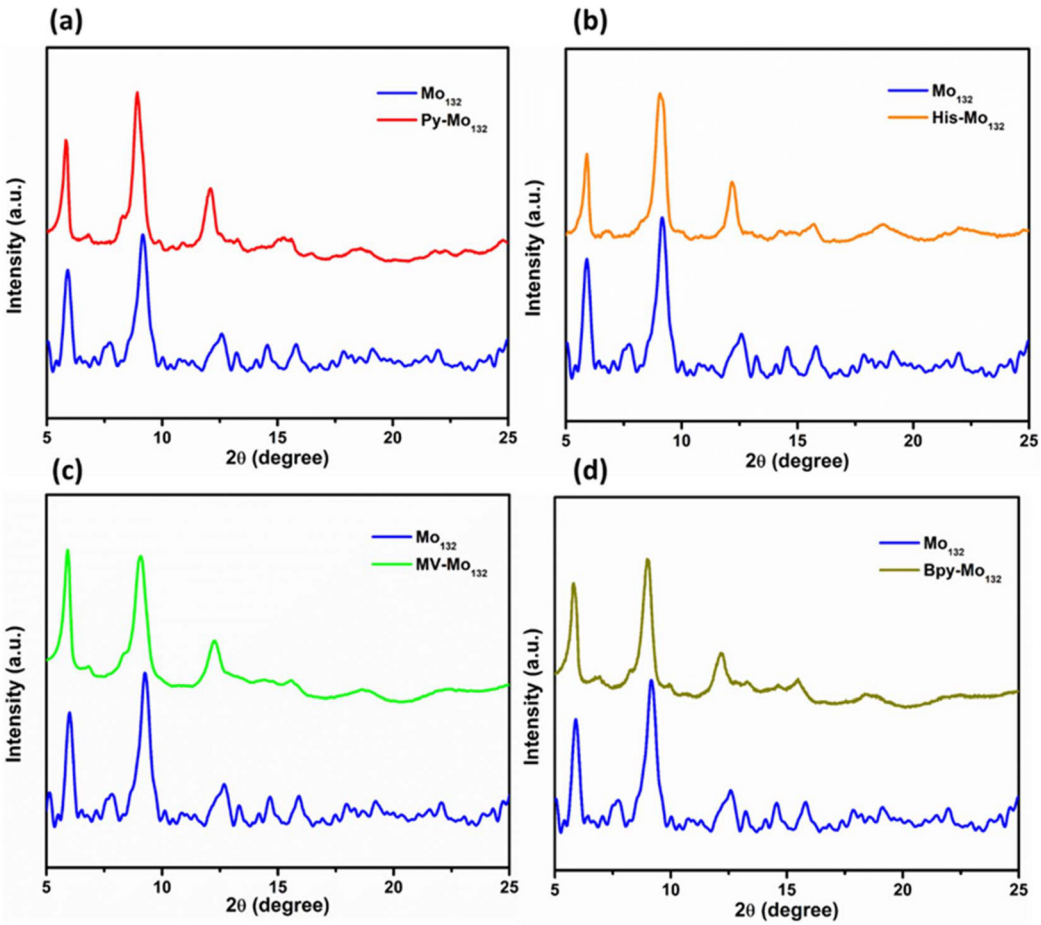

Fig. 2 Powder X-ray diffraction (PXRD) patterns for (a) **Py-Mo$_{132}$**, (b) **His-Mo$_{132}$**, (c) **MV-Mo$_{132}$** and (d) **Bpy-Mo$_{132}$** in comparison with that of pristine {Mo$_{132}$}.

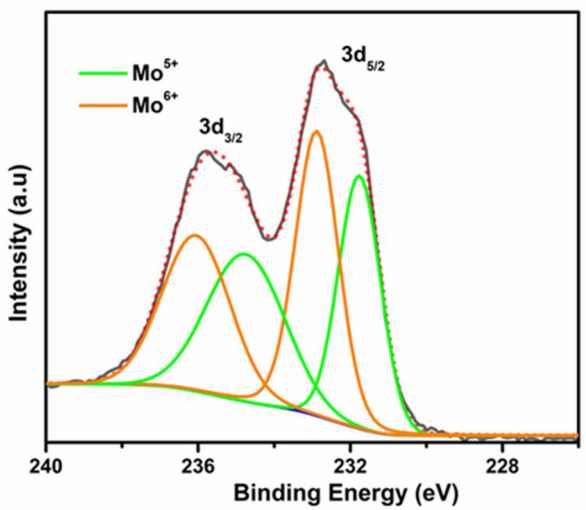

Fig. 3 XPS plot of **Py-Mo$_{132}$**.

To determine the oxidation state of Mo in the {Mo$_{132}$} cluster of the ion-exchanged products, X-ray photoelectron spectroscopy (XPS) was performed (Fig. 3 and Section S2.8, ESI†). The XPS plots for all the ion-exchanged products display the characteristic Mo 3d doublet consisting of $3d_{5/2}$ and $3d_{3/2}$ peaks. The spectra were deconvoluted using Lorentzian–Gaussian functions, enabling the identification of two sets of doublets corresponding to Mo^{V} and Mo^{VI} centers. Moreover, a quantitative analysis was conducted for determining the ratio between the peak areas corresponding to Mo^{V} and Mo^{VI}, and for all the products, the ratio was found to be approximately 1.2 : 1.[53] This proves that there are 72 Mo^{VI} and 60 Mo^{V} centers in the {Mo$_{132}$} cluster for all four ion-exchanged products, further substantiating the structural integrity of {Mo$_{132}$}.

The thermal stability of all four products and {Mo$_{132}$} was analyzed using thermogravimetry. Weight loss corresponding to water, both lattice and coordinated, can be observed in the range of 80–180 °C, for all the compounds (Fig. S12, ESI†). Beyond 220 °C and up until 380 °C, weight loss corresponding to the loss of organic cations and the degradation of the {Mo$_{132}$} ball can be observed for pristine {Mo$_{132}$} and **Py-Mo$_{132}$**. However, in the case of **MV-Mo$_{132}$** and **Bpy-Mo$_{132}$**, the degradation of the systems completes at ~450 °C, while for **His-Mo$_{132}$**, it completes at a much higher temperature of 550 °C.

The morphology of all the samples, **Py-Mo$_{132}$**, **His-Mo$_{132}$**, **Bpy-Mo$_{132}$**, and **MV-Mo$_{132}$**, was studied by field emission scanning electron microscopy (FESEM), as shown in Fig. 4. The FESEM image of the synthesized {Mo$_{132}$} is provided in Fig. S5 (ESI†). As can be seen from the images, the products are micro-crystalline in nature with crystallite sizes ranging from 0.2 μm for **Py-Mo$_{132}$** to 4 μm for **Bpy-Mo$_{132}$**.

Now, to determine the number of NH_4^+ ions that are partially exchanged with their respective organic cations to form **Py-Mo$_{132}$**, **His-Mo$_{132}$**, **Bpy-Mo$_{132}$**, and **MV-Mo$_{132}$**, ICP and CHN analyses were performed. According to the estimation, for every {Mo$_{132}$} anion in **His-Mo$_{132}$**, there are approximately 22 molecules of histidine (detailed data have been provided in the ESI, Sections S2.10 and S2.11†). Similarly, for **Py-Mo$_{132}$**, **MV-Mo$_{132}$** and **Bpy-Mo$_{132}$**, there are approximately 29 mole-

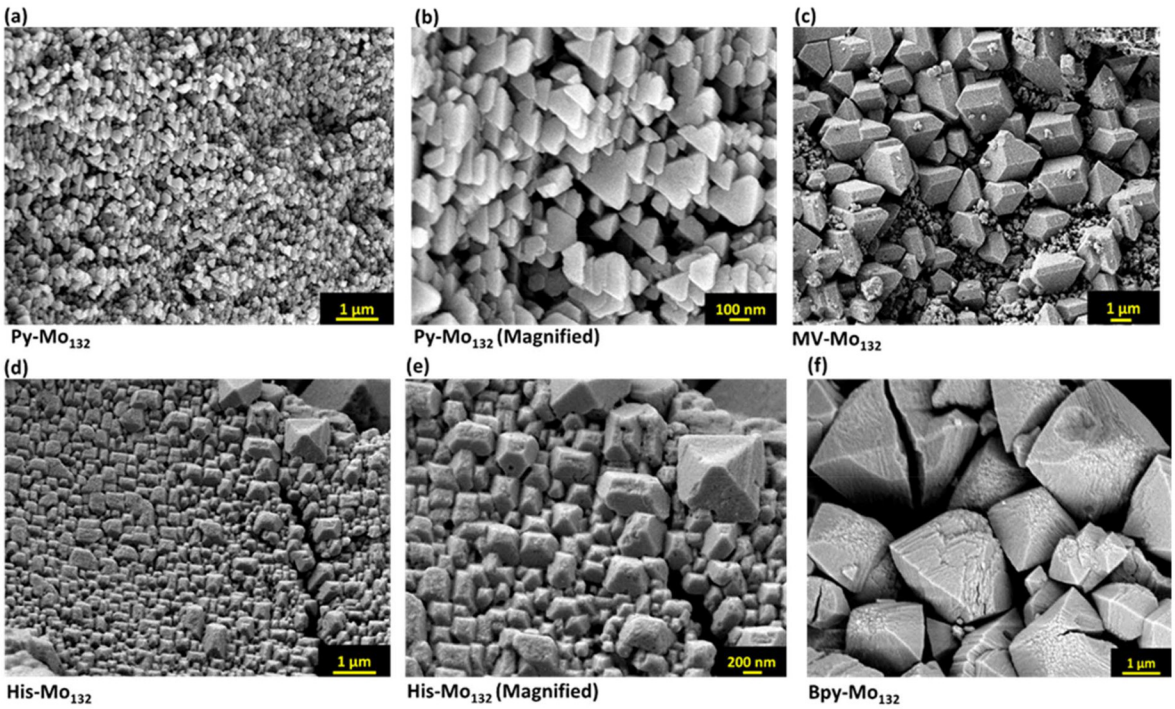

Fig. 4 FESEM images of **Py-Mo$_{132}$** (a and b), **MV-Mo$_{132}$** (c), **His-Mo$_{132}$** (d and e), and **Bpy-Mo$_{132}$** (f).

cules of pyridine, 14 molecules of methyl viologen, and 24 molecules of bipyridine, respectively, per formula unit. Here, it is to be noted that even though pyridine, bipyridine and histidine have one, two and three N-heteroatoms in the structure, respectively, their numbers being exchanged with the ammonium cations in $\{Mo_{132}\}$ are quite similar. While in the case of **MV-Mo$_{132}$**, the number of ions exchanged (14) is considerably lower than the rest of the ion exchanged products. Now, to understand this observation, we need to consider the pK_a values of the N-centers for all the organic molecules employed. The pK_a value of pyridine is 5.2, which means that at pH = 4.0, where the ion exchange reaction was performed, more than half of the pyridine concentration had been protonated. For bipyridine, the pK_a values are 2.5 and 4.9, which means that the concentration of mono-protonated species was much larger than that of di-protonated species at the pH of synthesis (that is, pH 4.0). In histidine, the carboxyl group has a pK_a value of 1.82, the amine group has a pK_a value of 9.3, and N-atom on the imidazole side chain has a pK_a value of 6. Thus, at pH 4, almost all the carboxyl groups and amine groups would have remained as $-COO^-$ and $-NH_3^+$, respectively, while most of the imidazole side chain would have been protonated. Due to such responses to pH, the numbers of exchanged cations for pyridinium, bipyridinium, and histidinium are closer to each other. However, for methyl viologen, which inherently exists in its dicationic form, almost half as many NH_4^+ cations were exchanged as in **Py-Mo$_{132}$**.

Proton conductivity studies

The samples **Py-Mo$_{132}$**, **His-Mo$_{132}$**, **Bpy-Mo$_{132}$**, and **MV-Mo$_{132}$** were studied for their proton conducting properties, using electrochemical impedance spectroscopy. The experiments were conducted using a two-electrode setup, under varying temperature and humidity conditions. The conductivity values were calculated by fitting the obtained Nyquist plots to the most suitable equivalent electrical circuit. A detailed description of the experiment methodology, along with the calculations, Nyquist plots, and the equivalent electrical circuit, are provided in the ESI (Section S2.12†). In brief, each sample was thoroughly ground into fine powder and then sandwiched between two carbon wafers to compress all of them into a pellet, under high pressure.[54]

The study of humidity-dependent proton conductivity of the samples was carried out in a humidity chamber, at a constant temperature of 45 °C, with relative humidity (RH) varying from 98% to 70%. The temperature-dependent proton conductivity studies were carried out at 98% RH by varying the temperature from 35 °C to 80 °C. Fig. 5a shows the Nyquist plot for **Py-Mo$_{132}$** at various temperatures and 98% relative humidity (RH). Nyquist plots for the other three compounds, **His-Mo$_{132}$**, **Bpy-Mo$_{132}$**, and **MV-Mo$_{132}$**, are provided in the ESI (Section S2.12†). The Nyquist plots for all the samples consist of an incomplete semicircle in the high frequency region, followed by a straight line in the lower frequency region, as shown in Fig. 5 and in Section S2.12 (ESI†).

The proton conductivity value for each sample was calculated from the resistance value obtained in the high frequency region of the respective Nyquist plots, which corresponds to the intrinsic resistance of that sample.[54,55] **Py-Mo$_{132}$** shows a conductivity of 3×10^{-3} S cm^{-1} at 35 °C, which increases to 1.07×10^{-2} S cm^{-1} at 80 °C and 98% RH. Similarly, the proton conductivity of the other samples also increases with an increase in temperature (complete data have been tabulated in the ESI; Tables S3, S5, S7 and S9†). **His-Mo$_{132}$**, **Bpy-Mo$_{132}$**, and **MV-Mo$_{132}$** show their highest conductivities of 6.7×10^{-3} S cm^{-1} (at 60 °C, 98% RH), 2×10^{-3} S cm^{-1} (at 80 °C, 98% RH), and 3.9×10^{-3} S cm^{-1} (at 80° C, 98% RH), respectively. Among these four compounds, **Py-Mo$_{132}$** shows the highest proton

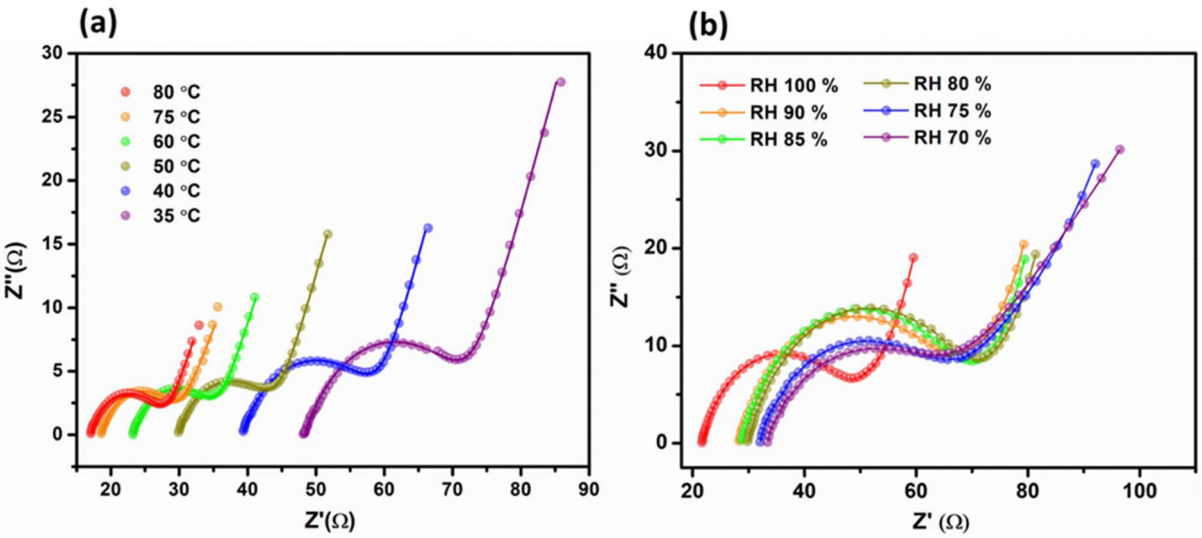

Fig. 5 Nyquist plots for **Py-Mo$_{132}$**: (a) at 98% relative humidity (RH) and at different temperatures; (b) at 45 °C and at different RH values. The solid lines represent the fitted data, and the points denote the experimental data.

conductivity (1.07×10^{-2} S cm^{-1}), followed by **His-Mo$_{132}$** (6.6×10^{-3} S cm^{-1}), **MV-Mo$_{132}$** (3.9×10^{-3} S cm^{-1}), and then **Bpy-Mo$_{132}$** (2×10^{-3} S cm^{-1}). The above-mentioned order is quite unexpected, since histidine having three N-heteroatoms and one carboxyl group was expected to facilitate building extensive H-bonded networks, thereby improving the proton conduction pathway. However, **His-Mo$_{132}$** is found to be structurally unstable above 60 °C. This might be because of the presence of the negatively charged carboxylate group on the alkyl side chain of the histidine ion. This negatively charged segment of histidine possibly faces electrostatic repulsion from the giant {Mo$_{132}$} cluster anion, ultimately lowering the structural stability and also the proton conductivity of the **His-Mo$_{132}$** product. On the other hand, between **Bpy-Mo$_{132}$** and **MV-Mo$_{132}$**, both of which have a similar structure, **MV-Mo$_{132}$** shows ~2 times higher conductivity than **Bpy-Mo$_{132}$**, throughout the temperature range of study. This is probably because in **Bpy-Mo$_{132}$**, bipyridine is mostly singly protonated and there are 24 of them, whereas in **MV-Mo$_{132}$**, there are 14 dicationic methyl viologens, which means that the organic content is higher in **Bpy-Mo$_{132}$** than in **MV-Mo$_{132}$**. Additionally, the non-protonated N-center in bipyridine probably does not interact with the {Mo$_{132}$} ball and therefore does not contribute to proton conduction. Another possible explanation for the higher conductivity of **Py-Mo$_{132}$** compared to the others could be the size of the organic cations. The {Mo$_{132}$} framework, with its cubic crystal system (*vide supra*), contains channels for proton conduction and a void space of approximately 5 Å. The pyridine molecule, being smaller (about 4.5 Å), likely fits within this void, allowing for closer interaction with {Mo$_{132}$} even from within the internal space (Fig. S27, ESI†). This advantage is not available to the other cations, which are larger than the void space in Mo$_{132}$, limiting their proximity and interaction with the {Mo$_{132}$} structure. Thus, **Py-Mo$_{132}$** containing the smallest of all – pyridinium cation – has the optimum interaction with the {Mo$_{132}$} ball, which results in **Py-Mo$_{132}$**, having the most efficient proton conductivity amongst all.

We have made this assumption because all the synthesized compounds crystallize in the cubic crystal system similar to parent {Mo$_{132}$} (referring to the similar PXRD patterns and unit cell parameters of **Py-Mo$_{132}$** and **His-Mo$_{132}$**). In order to understand the mechanism of proton conduction, Arrhenius plots were constructed for all the samples from the conductivity values at different temperatures. Fig. 6a shows Arrhenius plots for all four compounds. The activation energy for each of them was determined from the slopes of the Arrhenius plots as 0.24 eV, 0.18 eV, 0.27 eV, and 0.29 eV, for **Py-Mo$_{132}$**, **His-Mo$_{132}$**, **Bpy-Mo$_{132}$**, and **MV-Mo$_{132}$**, respectively. These values indicate that the proton conduction in all these compounds takes place predominantly through the Grotthuss mechanism. Here, it is noteworthy that these activation energies are much lower compared to previously reported {Mo$_{132}$}-based proton conductors (0.44–0.68 eV), which functioned predominantly through the vehicular mechanism.[48] A comparison among previously reported giant-POM based proton conductors and the materials reported in this present work has been tabulated in Table S12 (ESI†).

The dependence of proton conduction on relative humidity was also studied for all four compounds. Fig. 5b shows the Nyquist plots at 45 °C and at different relative humidity values for **Py-Mo$_{132}$**. The Nyquist plots and proton conductivity data for the other three compounds are provided in the ESI (Section S2.12†). Here, it is found that the values of proton conductivity increase sequentially with increasing humidity for each one of them (Fig. 6b; see also the ESI†). This indicates a water-assisted proton conduction process for all the samples in the present work. Among the four samples, **His-Mo$_{132}$** has the highest rate of increase in proton conduction with respect to RH (relative humidity), while **Bpy-Mo$_{132}$** shows the lowest rate of increase in proton conduction with increasing RH.

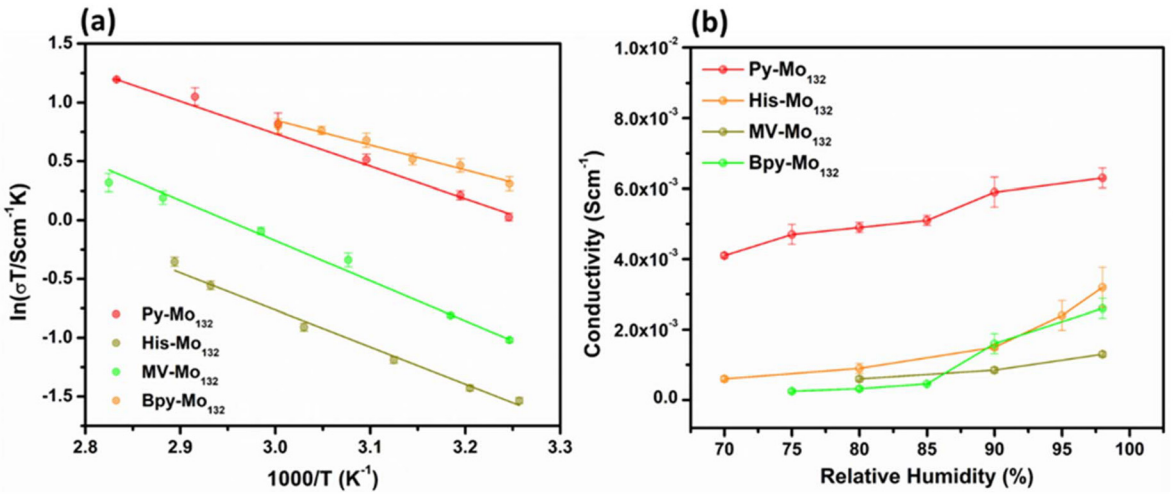

Fig. 6 (a) Arrhenius plots for activation energy and (b) humidity-dependent proton conductivity values for **Py-Mo$_{132}$**, **His-Mo$_{132}$**, **Bpy-Mo$_{132}$** and **MV-Mo$_{132}$**.

To gain a better overview of the role of humidity for the different samples, the dynamic vapour sorption (DVS) technique was used (Section S2.14, Fig. S28, ESI†). At 90% relative humidity (RH), **His-Mo$_{132}$** shows higher water uptake than **Py-Mo$_{132}$**. This is consistent with the expected behavior, as the additional heteroatoms and the carboxyl group in histidine contribute to its increased hydrophilicity. In hydrophilic materials, the affinity for water molecules supports the formation of a robust hydrogen-bonding network that facilitates proton transfer through the Grotthuss mechanism. In **His-Mo$_{132}$**, while elevated temperatures could enhance proton conductivity, this compound becomes unstable above 60 °C. This instability may stem from weaker interactions between histidine and the {Mo$_{132}$} cluster as mentioned earlier, which limits the compound's contribution to proton conduction at higher temperatures. Even though **His-Mo$_{132}$** exhibits a higher water uptake capacity, **Py-Mo$_{132}$** demonstrates more effective proton conductivity.

For a proton conductor functioning through the Grotthuss mechanism, the most crucial factors, which determine the efficiency of conduction, are the concentration and lability of protons. Therefore, to gain further insight into the observed trend of proton conductivity in the series of compounds synthesized, their acidity was determined. Here, the four compounds **Py-Mo$_{132}$**, **His-Mo$_{132}$**, **Bpy-Mo$_{132}$**, and **MV-Mo$_{132}$** were suspended in water by ultrasonication for 30 minutes and stirred overnight; thereafter, their acidity was measured. The pH observed for **Py-Mo$_{132}$**, **His-Mo$_{132}$**, **Bpy-Mo$_{132}$**, and **MV-Mo$_{132}$** is 3.5, 4.8, 5.0, and 4.5, respectively. According to this, proton conductivity of the compounds can be expected to be in the order of **Py-Mo$_{132}$** > **MV-Mo$_{132}$** > **His-Mo$_{132}$** > **Bpy-Mo$_{132}$**, which matches more or less well with the observed trend (**Py-Mo$_{132}$** > **His-Mo$_{132}$** > **MV-Mo$_{132}$** > **Bpy-Mo$_{132}$**), except for the fact that **His-Mo$_{132}$** shows a higher proton conductivity value than that of **MV-Mo$_{132}$**, which is the opposite trend predicted by the pH values of the respective compounds' aqueous suspensions. We can explain this anomaly by considering the lowest activation energy (0.18 eV) of **His-Mo$_{132}$** towards its proton conduction compared to the highest activation energy (0.29 eV) of **MV-Mo$_{132}$** towards its proton conduction. Upon comparing the trend of activation energy among the products, a direct correlation can be observed with the water sorption results obtained from dynamic vapor sorption (DVS) analysis (Fig. S28, ESI†). The amount of water adsorbed per formula unit of the ion-exchanged product is **His-Mo$_{132}$** (137) > **Py-Mo$_{132}$** (105) > **Bpy-Mo$_{132}$** (92) > **MV-Mo$_{132}$** (78). This implies that higher uptake of water molecules lowers the activation energy barrier for proton transport in these samples.

Furthermore, to check the stability of these {Mo$_{132}$}-based proton conductors under the operational conditions, impedance measurements were conducted for all four products, during the subsequent heating–cooling cycling. All four compounds, **Py-Mo$_{132}$**, **His-Mo$_{132}$**, **MV-Mo$_{132}$**, and **Bpy-Mo$_{132}$**, were stable up to the 3rd cycle (Fig. 7). The Nyquist plots for each cycle are provided in the ESI (Section S2.12, ESI†). Furthermore, the pellets of all the samples after impedance measurements were ground, and the material stability was analyzed by PXRD (Fig. S29, ESI†) and IR spectroscopy

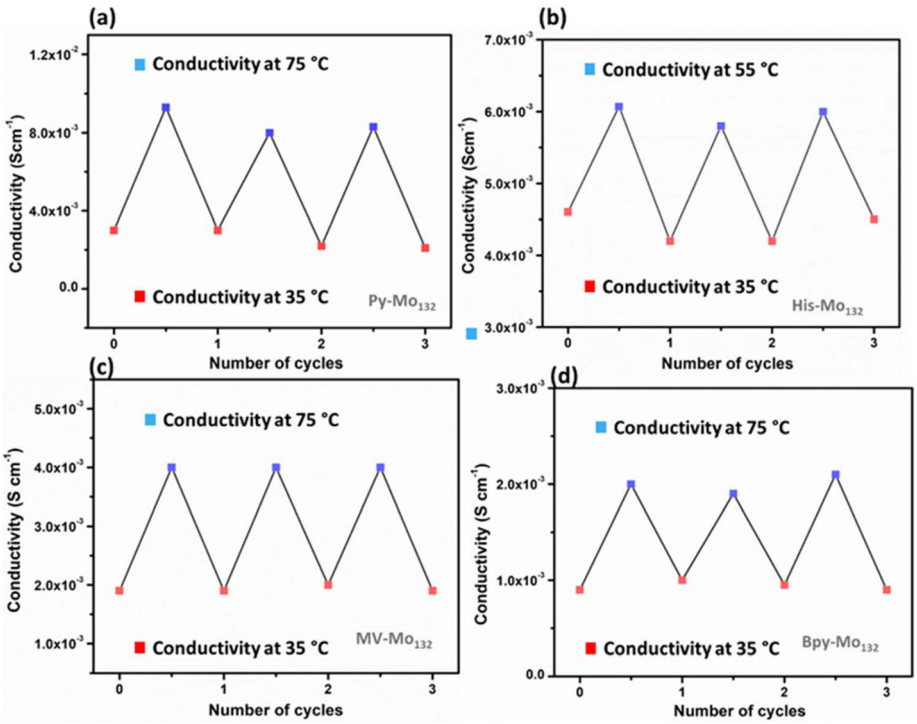

Fig. 7 Proton conductivity during the heating–cooling cycles of (a) **Py-Mo$_{132}$**, (b) **His-Mo$_{132}$**, (c) **MV-Mo$_{132}$** and (d) **Bpy-Mo$_{132}$**.

(Fig. S30, ESI†). The characterization results obtained after the impedance measurements were in good agreement with the data that was acquired prior to the measurement, which indicates the retention of structural integrity for **Py-Mo$_{132}$**, **His-Mo$_{132}$**, and **MV-Mo$_{132}$**. Additionally, the electrical conductivity of all the products was also analyzed using direct current, since it is important that for a material to be used in proton exchange membranes, it should be electronically non-conducting. The relevant experimental details, the results obtained and the calculations are provided in the ESI (Section S2.16†). For all the products, the conductivity was found to be very low (10^{-7}–10^{-8} S cm^{-1}), which indicates that the conductivity observed for the materials in higher humidity (10^{-3} S cm^{-1}) primarily originates from the conduction of protons assisted by water molecules.

Conclusion

In summary, we have successfully synthesized water-insoluble proton conductors based on the giant POM {Mo$_{132}$} by exchanging its ammonium cations with larger organic cations—pyridinium, histidinium, bipyridinium, and methyl viologen—resulting in **Py-Mo$_{132}$**, **His-Mo$_{132}$**, **Bpy-Mo$_{132}$** and **MV-Mo$_{132}$**, respectively. The organic molecules used have varying numbers of N-heteroatoms, and their differing pK_a values affect the extent of protonation. Among these compounds, **Py-Mo$_{132}$** exhibits the highest proton conductivity, reaching 1.07×10^{-2} S cm^{-1} at 80 °C and 98% relative humidity.

Our findings indicate that by increasing the number of heteroatoms in the cations, the water uptake capacity and activation energy of the products could be improved. However, for obtaining stable proton conductivity, an optimal interaction between the cations and the giant {Mo$_{132}$} anion might play a crucial role. These proton conductors primarily operate *via* the Grotthuss mechanism and demonstrate stability up to 80 °C. This study underscores the potential of the giant POM {Mo$_{132}$} as a promising candidate for developing proton conductors suitable for fuel cell applications.

Data availability

The data supporting this article, including experimental procedures, instrumentation details, characterization studies (including FT-IR, UV-Vis and XPS spectroscopy, TGA and elemental analysis), detailed proton conductivity studies (including Nyquist plots, equivalent circuit and proton conductivity calculations, and post-impedance material analysis), electrical conductivity study, and comparison of the proton conductivity of previously reported POMs, have been included in the ESI.†

Conflicts of interest

The authors declare no conflict of interest.

Acknowledgements

We thank Chaitanya D and Prof. Ashwini Nangia (School of Chemistry, University of Hyderabad) for helping us with the DVS measurements. We thank Prof. Rajeev Gupta (University of Delhi) and Dr Ujjwal Pal (Principal Scientist, IICT, Hyderabad) for helping us with the CHN analyses. We also thank Ingilala Venkataramanaiah from the School of Physics for helping us with the Raman analysis and the School of Physics for use of the PXRD facilities. We are thankful to IoE-UoH (Project No. RC1-20-007) and SERB, DST, Government of India (Project No. CRG/2022/007283) for the financial assistance. P. M. U. thanks DST-INSPIRE, New Delhi, India, and O. B. thanks UGC, New Delhi, India, for their fellowships and R. N. thanks UGC, Government of India, for the Dr D. S. Kothari Post-doctoral fellowship (F.4-2/2006 (BSR)/CH/18-19/0032). We thank Calicut University, IISER Bhopal, and SAIF-IIT Madras, for providing the instrumental facility for the CHN and ICP-OES elemental analyses. S. K. D. thanks the Science and Engineering Research Board (SERB), DST, Government of India, for the J. C. Bose fellowship (JCB/2023/000007).

References

1 B. C. H. Steele and A. Heinzel, *Nature*, 2001, **414**, 345–352.
2 M. Z. Jacobson, W. G. Colella and D. M. Golden, *Science*, 2005, **308**, 1901–1905.
3 A. B. Stambouli and E. Traversa, *Energy Rev.*, 2002, **6**, 295–304.
4 E. Fabri, D. Pergolesi and E. Traversa, *Chem. Soc. Rev.*, 2010, **39**, 4355–4369.
5 M. E. Scofield, H. Liu and S. S. Wong, *Chem. Soc. Rev.*, 2015, **44**, 5836–5860.
6 S. Pili, S. P. Argent, C. G. Morris, P. Rought, V. García-Sakai, I. P. Silverwood, T. L. Easun, M. Li, M. R. Warren, C. A. Murray, C. C. Tang, S. Yang and M. Schröder, *J. Am. Chem. Soc.*, 2016, **138**, 6352–6355.
7 P. Ramaswamy, N. E. Wong and G. K. H. Shimizu, *Chem. Soc. Rev.*, 2014, **43**, 5913–5932.
8 A. Kraytsberg and Y. Ein-Eli, *Energy Fuels*, 2014, **28**, 7303–7330.
9 A. Kusoglu and A. Z. Weber, *Chem. Rev.*, 2017, **117**, 987–1104.
10 Y. Kim, K. Ketpang, S. Jaritphun, J. S. Park and S. Shanmugam, *J. Mater. Chem. A*, 2015, **3**, 8148–8155.
11 K. A. Mauritz and R. B. Moore, *Chem. Rev.*, 2004, **104**, 4535–4586.
12 K. D. Kreuer and G. A. Portale, *Adv. Funct. Mater.*, 2013, **23**, 5390–5397.
13 X. Meng, H. N. Wang, S. Y. Song and H. J. Zhang, *Chem. Soc. Rev.*, 2017, **46**, 464–480.
14 M. T. Pope and A. Muller, *Angew. Chem., Int. Ed. Engl.*, 1991, **30**, 34–48.
15 C. L. Hill, *Chem. Rev.*, 1998, **98**, 1–2.

16 A. Proust, R. Thouvenot and P. Gouzerh, *Chem. Commun.*, 2008, 1837–1857.
17 L. Cronin and A. Muller, *Chem. Soc. Rev.*, 2012, **41**, 7333–7334.
18 L. V. Nadal and L. Cronin, *Nat. Rev. Mater.*, 2017, **2**, 17054.
19 S. Uchida, *Chem. Sci.*, 2019, **10**, 7670–7679.
20 A. Misra, K. Kozma, C. Streb and M. Nyman, *Angew. Chem., Int. Ed.*, 2020, **59**, 596–612.
21 D. W. Lim and H. Kitagawa, *Chem. Rev.*, 2020, **120**, 8416–8467.
22 H. B. Luo, Q. Ren, P. Wang, J. Zhang, L. Wang and X. M. Ren, *Appl. Mater. Interfaces*, 2019, **11**, 9164–9171.
23 R. Sahoo, S. Mondal, S. C. Pal, D. Mukherjee and M. C. Das, *Adv. Energy Mater.*, 2021, **11**, 2102300.
24 C. Fan, H. Geng, H. Wu, Q. Peng, X. Wang, B. Shi, Y. Kong, Z. Yin, Y. Liu and Z. Jiang, *J. Mater. Chem. A*, 2021, **9**, 17720–17723.
25 X. Wu, Y. L. Hong, B. Xu, Y. Nishiyama, W. Jiang, J. Zhu, G. Zhang, S. Kitagawa and S. Horike, *J. Am. Chem. Soc.*, 2020, **142**, 14357–14364.
26 J. Yagyu, M. S. Islam, Y. Shudo, M. Fukuda, H. Ushijima, J. Ohyama, S. Ida, L. F. Lindoy and S. Hayami, *Appl. Energy Mater.*, 2021, **4**, 6296–6301.
27 M. R. Karim, K. Hatakeyama, T. Matsui, H. Takehira, T. Taniguchi, M. Koinuma, Y. Matsumoto, T. Akutagawa, T. Nakamura, S.-i. Noro, T. Yamada, H. Kitagawa and S. Hayami, *J. Am. Chem. Soc.*, 2013, **135**, 8097–8100.
28 T. Murakami, J. R. Hester and M. Yashima, *J. Am. Chem. Soc.*, 2020, **142**, 11653–11657.
29 W. Zhang and Y. H. Hu, *Energy Sci. Eng.*, 2021, **9**, 984–1011.
30 O. Nakamura, T. Kodama, I. Ogino and Y. Miyake, *Chem. Lett.*, 1979, **8**, 17–18.
31 O. Nakamura, I. Ogino and T. Kodama, *Solid State Ionics*, 1981, **3–4**, 347–351.
32 H. Y. Wang, S. R. Li, X. Wang, L. S. Long, X. J. Kong and L. S. Zheng, *Sci. China:Chem.*, 2021, **64**, 959–963.
33 S. Mulkapuri, S. K. Kurapati, S. Mukhopadhyay and S. K. Das, *New J. Chem.*, 2019, **43**, 17670–17679.
34 J. Lin, N. Li, S. Yang, M. Jia, J. Liu, X. M. Li, L. An, Q. Tian, L. Z. Dong and Y. Q. Lan, *J. Am. Chem. Soc.*, 2020, **142**, 13982–13988.
35 K. Tandekar, C. Singh and S. Supriya, *Eur. J. Inorg. Chem.*, 2021, 734–739.
36 Z. Li, L. D. Lin, H. Yu, X. X. Li and S. T. Zheng, *Angew. Chem., Int. Ed.*, 2018, **57**, 15777–15781.
37 J. C. Liu, Q. Han, L. J. Chen, J. W. Zhao, C. Streb and Y. F. Song, *Angew. Chem., Int. Ed.*, 2018, **57**, 8416–8420.
38 T. Iwano, K. Shitamatsu, N. Ogiwara, M. Okuno, Y. Kikukawa, S. Ikemoto, S. Shirai, S. Muratsugu, P. G. Waddell, R. J. Errington, M. Sadakane and S. Uchida, *Appl. Mater. Interfaces*, 2021, **13**, 19138–19147.
39 P. Yang, M. Alsufyani, A. H. Emwas, C. Chen and N. M. Khashab, *Angew. Chem., Int. Ed.*, 2018, **57**, 13046–13051.
40 B. Liu, D. Cheng, H. Zhu, J. Du, K. Li, H. Y. Zang, H. Tan, Y. Wang, W. Xing and Y. Li, *Chem. Sci.*, 2019, **10**, 556–563.
41 Z. W. Guo, Y. D. ChenZhao, Y. L. Wu, L. D. Lin and S. T. Zheng, *Inorg. Chem.*, 2019, **58**, 4055–4058.
42 S. Farhadi and M. Zaidi, *Appl. Catal., A*, 2009, **354**, 119–126.
43 A. Maldotti, A. Molinari and F. Bigi, *J. Catal.*, 2008, **253**, 312–317.
44 Y. Guo, Y. Wang, C. Hu, Y. Wang, E. Wang, Y. Zhou and S. Feng, *Chem. Mater.*, 2000, **12**, 3501–3508.
45 H. Park and W. Choi, *Catal. Today*, 2005, **101**, 291–297.
46 A. Müller, E. Krickemeyer, H. Bögge, M. Schmidtmann and F. Peters, *Angew. Chem., Int. Ed.*, 1998, **37**, 3359–3363.
47 E. Haviv, B. Chen, R. Carmieli, L. Houben, H. Cohen, G. Leitus, L. Avram and R. Neumann, *J. Am. Chem. Soc.*, 2020, **142**, 14504–14512.
48 W. J. Liu, L. Z. Dong, R. H. Li, Y. J. Chen, S. N. Sun, S. L. Li and Y. Q. Lan, *ACS Appl. Mater. Interfaces*, 2019, **11**, 7030–7036.
49 A. Misra, K. Kozma, C. Streb and M. Nyman, *Angew. Chem., Int. Ed.*, 2020, **59**, 596–612.
50 S. Biswas, D. Melgar, A. Srimany, A. R. Fortea, T. Pradeep, C. Bo, J. M. Poblet and S. Roy, *Inorg. Chem.*, 2016, **55**, 8285–8291.
51 C. Schaffer, A. M. Todea, P. Gouzerh and A. Muller, *Chem. Commun.*, 2012, **48**, 350–352.
52 S. Xu, Y. Wang, Y. Zhao, W. Chen, J. Wang, L. He, Z. Su, E. Wang and Z. Kang, *J. Mater. Chem. A*, 2016, **4**, 14025–14032.
53 Y. Zhou, Z. Shi, L. Zhang, S. Hassan and N. Qu, *Appl. Phys. A*, 2013, **113**, 563–568.
54 S. Mukhopadhyay, J. Debgupta, C. Singh, R. Sarkar, O. Basu and S. K. Das, *ACS Appl. Mater. Interfaces*, 2019, **11**, 13423–13432.
55 O. Basu, S. Mukhopadhyay, S. Laha and S. K. Das, *Chem. Mater.*, 2022, **34**, 6734–6743.